Article

Electronic and Optical Properties of Atomic-Scale Heterostructure Based on MXene and MN (M = Al, Ga): A DFT Investigation

Kai Ren [1,*], Ruxin Zheng [1], Peng Xu [1], Dong Cheng [1], Wenyi Huo [1], Jin Yu [2], Zhuoran Zhang [3] and Qingyun Sun [1,*]

[1] School of Mechanical and Electronic Engineering, Nanjing Forestry University, Nanjing 210037, China; Ruxin.Zheng@institutionalemail.cn (R.Z.); Peng.Xu@institutionalemail.cn (P.X.); dongtian176@163.com (D.C.); WenyiHuo@institutionalemail.cn (W.H.)

[2] School of Materials Science and Engineering, Southeast University, Nanjing 211189, China; JinYu@institutionalemail.cn

[3] Center for More-Electric-Aircraft Power System, Nanjing University of Aeronautics and Astronautics, Nanjing 211106, China; Zhuoran.Zhang@institutionalemail.cn

* Correspondence: author: kairen@njfu.edu.cn (K.R.); sunqingyun@njfu.edu.cn (Q.S.)

Abstract: After the discovery of graphene, a lot of research has been conducted on two-dimensional (2D) materials. In order to increase the performance of 2D materials and expand their applications, two different layered materials are usually combined by van der Waals (vdW) interactions to form a heterostructure. In this work, based on first-principles calculation, some charming properties of the heterostructure constructed by Hf_2CO_2, AlN and GaN are addressed. The results show that Hf_2CO_2/AlN and Hf_2CO_2/GaN vdW heterostructures can keep their original band structure shape and have strong thermal stability at 300 K. In addition, the Hf_2CO_2/MN heterostructure has I-type band alignment structure, which can be used as a promising light-emitting device material. The charge transfer between the Hf_2CO_2 and AlN (or GaN) monolayers is 0.1513 (or 0.0414) $|e|$. The potential of Hf_2CO_2/AlN and Hf_2CO_2/GaN vdW heterostructures decreases by 6.445 eV and 3.752 eV, respectively, across the interface. Furthermore, both Hf_2CO_2/AlN and Hf_2CO_2/GaN heterostructures have remarkable optical absorption capacity, which further shows the application prospect of the Hf_2CO_2/MN heterostructure. The study of this work provides theoretical guidance for the design of heterostructures for use as photocatalytic and photovoltaic devices.

Keywords: two-dimensional materials; Hf_2CO_2; heterostructure; first-principles calculation

1. Introduction

Since 2004, Novoselov and Geim prepared graphene from graphite by the mechanical exfoliation method [1], and its remarkable physical and chemical properties were explored [2–11], which also attracted extensive interest and attention on other two-dimensional (2D) materials, and they all show fantastic properties [12–17]. For example, black phosphorene is a honeycomb-like folded layered material that can achieve transistor performance with a thickness of less than 7.5 nm, and the highest carrier mobility can be obtained by 1000 cm^2/V·s when the thickness is 10 nm at room temperature [18–21]. Puckered arsenene possesses the ability to adjust its bandgap by applying the external strain on its surface. Interestingly, arsenene can even be transformed into a straight gap semiconductor by applying 1% strain [22–27]. Transition metal dichalcogenides (TMDs) materials are layered materials with excellent thermal [28,29], electronic [30] and optical properties [31]. For instance, MoS_2 has high broadband gain (up to 13.3), detection rate (up to 10^{10} cm $Hz^{1/2}$/W) and high thermal stability when using it as an optoelectronic device [32]. In addition, there are Janus TMDs materials that destroy the symmetry of the original structure and make its carrier mobility increase from 28 to 606 cm^2/V·s [33]. The Janus MoSSe material

is able to separate light-generated electrons and holes while also exhibiting perfect light absorption capabilities, which lays the foundation for promoting water redox reactions, and it is a remarkable water decomposition light catalyst [34]. The novel properties of these 2D materials can provide unprecedented help for the development of nano-devices and solar cells [35,36].

In order to expand the application of 2D materials and build more special performances, superposing different layered materials to construct a heterostructure is usually realized [37–43]. Especially, two-layer materials construct a heterostructure by van der Waals (vdW) forces, which can induce novel interfacial [44], optical [45] and electronic properties [46]. The SiC/TMDs vdW can be used as a water decomposition catalyst to completely separate hydrogen and oxygen under the condition of light [47]. The PbSe/CdSe heterostructure has near infrared emission characteristics, which is closely related to its type-I alignment band [48]. The average carrier value of the type-I PbI_2/WS_2 layered heterostructure is 0.039 $cm^2 \cdot s^{-1}$, and it is found that the interlayer diffusion behavior between electrons and holes is similar [49]. These investigations have demonstrated that type-I heterostructures possess promising applications in photocatalytic, photovoltaic and optical devices [50,51]. Recently, layered MAX phases have been exfoliated into monolayer and multilayers, named MXenes, which has attracted wide attention [52]. The charming electrochemical [53], conductive [54] and stable capacity [55] characteristics provide potential applications in electrocatalysts, photocatalysts and energy storage devices [56–58]. Although most of the MXenes are metallic, some MXenes are semiconductors with a desirable bandgap [59,60]. In particular, the Cr_2TiC_2 monolayer behaves as a novel bipolar antiferromagnetic semiconductor showing opposite spin directions, which can be used as antiferromagnetic spin field effect transistor [61]. Hf_2CO_2 possesses excellent electronic and thermoelectric properties and carrier mobility (about 1531.48 $cm^2/V \cdot s$ for electrons), suggesting an efficient photocatalyst for water splitting and nano-electronic devices [62–66], and this novel electronic characteristic can even be tuned by external strain [67]. Hf_2CO_2 is also sensitive to NH_3, which can sharply enhance electronic conductivity [68]. More recently, MN (M = Al, Ga) has been reported to have remarkable optical, electronic and mechanical properties, and it can be considered as a candidate for future optical and photovoltaic devices [69–75]. Interestingly, the prepared 2D AlN shows great promise in deep-ultraviolet optoelectronic applications, ultraviolet LEDs and laser diodes [76,77]. In addition, 2D GaN is also fabricated by epitaxial graphene using a migration-enhanced encapsulated growth method [75], and is studied as a decent semiconductor for heterostructures [78], photocatalysts [79] and photocathodes [80]. Moreover, some Hf_2CO_2 and MN-based heterostructures have been reported, such as Hf_2CO_2/WS_2 [62], Hf_2CO_2/blue phosphorene [65], MoS_2/MN [81], GeC/GaN [82], etc., while studies of the Hf_2CO_2/MN heterostructure are still limited. Therefore, considering such fantastic electronic properties of Hf_2CO_2, and the synthesized MN (M = Al, Ga), it is worth constructing the heterostructure by Hf_2CO_2 and MN to explore the novel performances and the potential applications.

In this study, the first-principles method was utilized to investigate the formed heterostructure based on Hf_2CO_2 and MN (M = Al, Ga). The binding energy and the ab initio molecular dynamics (AIMD) calculations were conducted to check the stability of the heterostructure. Furthermore, the type-I band alignment of the Hf_2CO_2/MN heterostructure was addressed, which demonstrates the potential applications of the light-emitting devices. In addition, the charge difference between the MXene and the MX layers was studied and the potential drop was also calculated to develop the interfacial properties of the heterostructure. Moreover, the light absorption capacity of the Hf_2CO_2/MN heterostructure was obtained by calculating the intrinsic optical absorption spectrum.

2. Computing Method

The method of calculations in this work was based on density functional theory (DFT), implemented by first-principles simulation under the circumstances of the Vienna *ab initio*

simulation package (VASP) [83]. Based on generalized gradient approximation (GGA), the Perdew–Burke–Ernzerhof (PBE) functional was employed for the explanation of the exchange correlation functional [84–86]. For the more precise bandgap results, we used the hybrid Heyd–Scuseria–Ernzerhof (HSE06; screening parameter 0.2 Å^{-1}, mixing parameter 0.25) simulations [87] and the DFT-D3 method of Grimme, and the dipole corrections were also used to correct the weak dispersion forces. A tested 500 eV cutoff energy was considered. After the convergence test for the *k*-point (seen in Table S1 of Supplementary Materials), the Monkhorst–Pack *k*-point of $7 \times 7 \times 1$ was adopted to relax the structure, while the static and optical calculations were conducted by the $11 \times 11 \times 1$ *k*-point. For the prevention of the interaction of the adjacent atomic layers, the vacuum slab was controlled by 25 Å. Furthermore, the energy of the calculated materials in this work was set within 1×10^{-5} eV, while the Hellmann–Feynman forces on the atoms were set to less than 0.01 eV·Å^{-1}.

3. Results and Discussions

We first optimized the structures of Hf$_2$CO$_2$, AlN and GaN, and the top and side views of the crystal structure and band energy for the Hf$_2$CO$_2$, AlN and GaN monolayers are shown in Figure 1a–c, respectively. The lattice constants of monolayered Hf$_2$CO$_2$ AlN and GaN are obtained by 3.363, 3.127 and 3.255 Å, respectively. In addition, the bond lengths of Hf−C, Hf−O, Al−N and Ga−N in Hf$_2$CO$_2$, AlN and GaN monolayers are 2.369, 2.132, 1.805 and 1.895 Å, respectively. In addition, the HSE06 method-calculated energy band structures of Hf$_2$CO$_2$, AlN and GaN monolayers show that all these layered materials have semiconductor features with the bandgaps of 1.820, 4.042 and 3.203 eV, respectively. For the Hf$_2$CO$_2$ monolayer, the conduction band minimum (CBM) is located at the M point, while the valence band maximum (VBM) appears at the Γ point. The CBM and VBM of AlN (or GaN) are generated at the Γ point and K point, respectively. All these calculated results are almost the same as the previous investigation results [65,66,88].
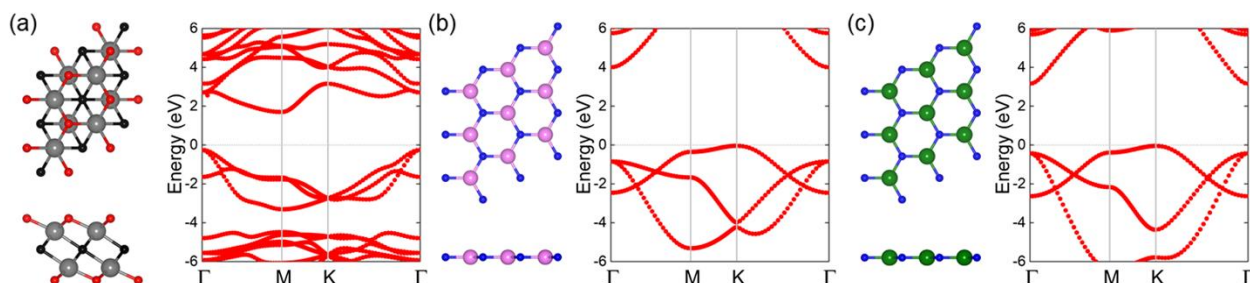

Figure 1. The atomic structure and the band structure of the (**a**) Hf$_2$CO$_2$, (**b**) AlN and (**c**) GaN monolayers. The grey, red, black, pink, green and blue marks are Hf, O, C, Al, Ga and N atoms, respectively, and the Fermi energy level is 0, shown by gray dashes.

To construct the heterostructure by Hf$_2$CO$_2$ and MN (N = Al, Ga) monolayers, the six most representative stacking configurations, shown in Figure 2, should be taken into consideration. In the six Hf$_2$CO$_2$/MN heterostructures, the binding energy (E_{binding}) of the Hf$_2$CO$_2$/MN heterostructure is decided by:

$$E_{\text{binding}} = E_{\text{MXene/MN}} - E_{\text{MXene}} - E_{\text{MN}} \tag{1}$$

where $E_{\text{MXene/MN}}$, E_{MXene} and E_{MN} show the total energy of the Hf$_2$CO$_2$/MN heterostructure, monolayered Hf$_2$CO$_2$ and MN, respectively. The smaller the binding energy, the more stable the structure of the heterostructure [89], and thus the most stable structure of those six stacking configurations of the heterostructure is decided as the lowest binding energy, which is demonstrated in the AA stacking style of the Hf$_2$CO$_2$/MN heterostructure. The calculated E_{binding} of the Hf$_2$CO$_2$/AlN and Hf$_2$CO$_2$/GaN heterostructures with the most stable configuration is −56.98 and −52.44 meV/Å^{-2}, respectively, in Table 1. It is worth not-

ing that the framework of the quantum theory of atoms in molecules (QTAIM) functional is not considered here, which is also a popular method for simulations [90–99]. The results show that the Hf_2CO_2/MN heterostructure is formed by vdW interactions [100,101]. For the most stable Hf_2CO_2/AlN and Hf_2CO_2/GaN vdW heterostructures, the bond lengths of Hf−C, Hf−O and M−N are slightly changed compared with original layered materials, which further proves the weak vdW forces between the interface of the heterostructures. In addition, the interface distances of the Hf_2CO_2/AlN and Hf_2CO_2/GaN vdW heterostructures are 1.924 and 2.235 Å, respectively. Additionally, in the following sections, we only discuss the most stable Hf_2CO_2/MN heterostructure stacking structure.

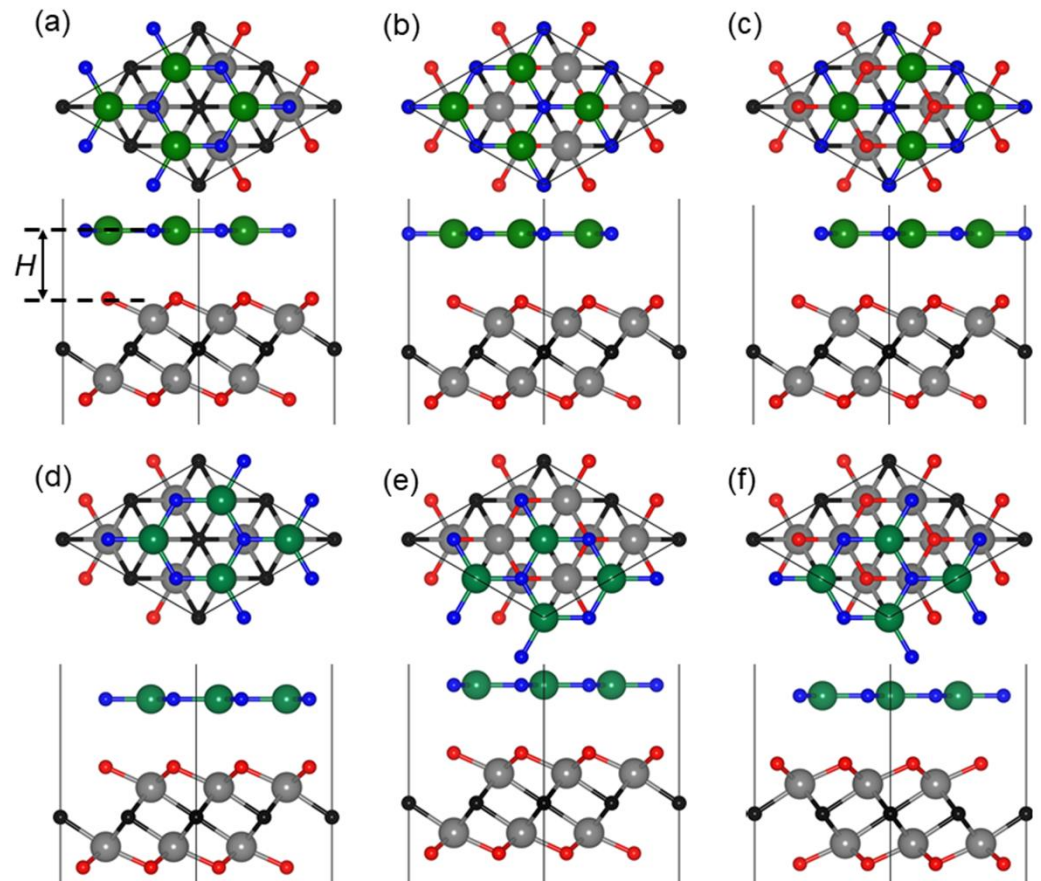**Figure 2.** Top and side views of the (**a**) AA, (**b**) AB, (**c**) AC, (**d**) AD, (**e**) AE and (**f**) AF stacking configurations of the Hf_2CO_2/MN heterostructure.

Table 1. The optimized lattice parameter (*a*, Å), bond length (B, Å), binding energy ($E_{binding}$, meV/Å^{-2}), interface height (*H*, Å) and bandgap (E_g, eV) obtained by HSE06 method for the Hf_2CO_2, AlN, GaN monolayers and Hf_2CO_2/AlN, Hf_2CO_2/GaN heterostructures.

	a	$B_{Hf–C}$	$B_{Hf–O}$	$B_{M–N}$	$E_{binding}$	*H*	E_g
Hf_2CO_2	3.363	2.369	2.132				1.820
AlN	3.127			1.805			4.042
GaN	3.283			1.895			3.203
Hf_2CO_2/AlN	3.328	2.354	2.121	1.922	−56.98	1.924	1.826
Hf_2CO_2/GaN	3.329	2.355	2.101	1.922	−52.44	2.235	1.734

In order to further investigate the thermal stability of the Hf_2CO_2/MN vdW heterostructure, AIMD simulations were explored for the Hf_2CO_2/MN vdW heterostructure by the Nosé–Hoover heat bath scheme [102]. To consider the constraints of the lattice translation, we constructed a $6 \times 6 \times 1$ supercell for the Hf_2CO_2/AlN and Hf_2CO_2/GaN vdW

heterostructures in the AIMD simulation, which contained 252 atoms in total. The ambient temperature of the simulation was set as 300 K, and the structures of the Hf_2CO_2/AlN and Hf_2CO_2/GaN vdW heterostructures after relaxation for 5 ps are shown in Figure 3a,c, respectively. The simulation results of AIMD show that the structures of the Hf_2CO_2/AlN and Hf_2CO_2/GaN vdW heterostructures still remain intact after 5 ps under 300 K, revealing the robust thermal stability of the heterostructure. In addition, as shown in Figure 3b,d, the total energy fluctuation and simulation time for Hf_2CO_2/AlN and Hf_2CO_2/GaN vdW heterostructures in AIMD calculation are demonstrated, respectively, and they all show the convergence state by time, ensuring the reliability of the results.
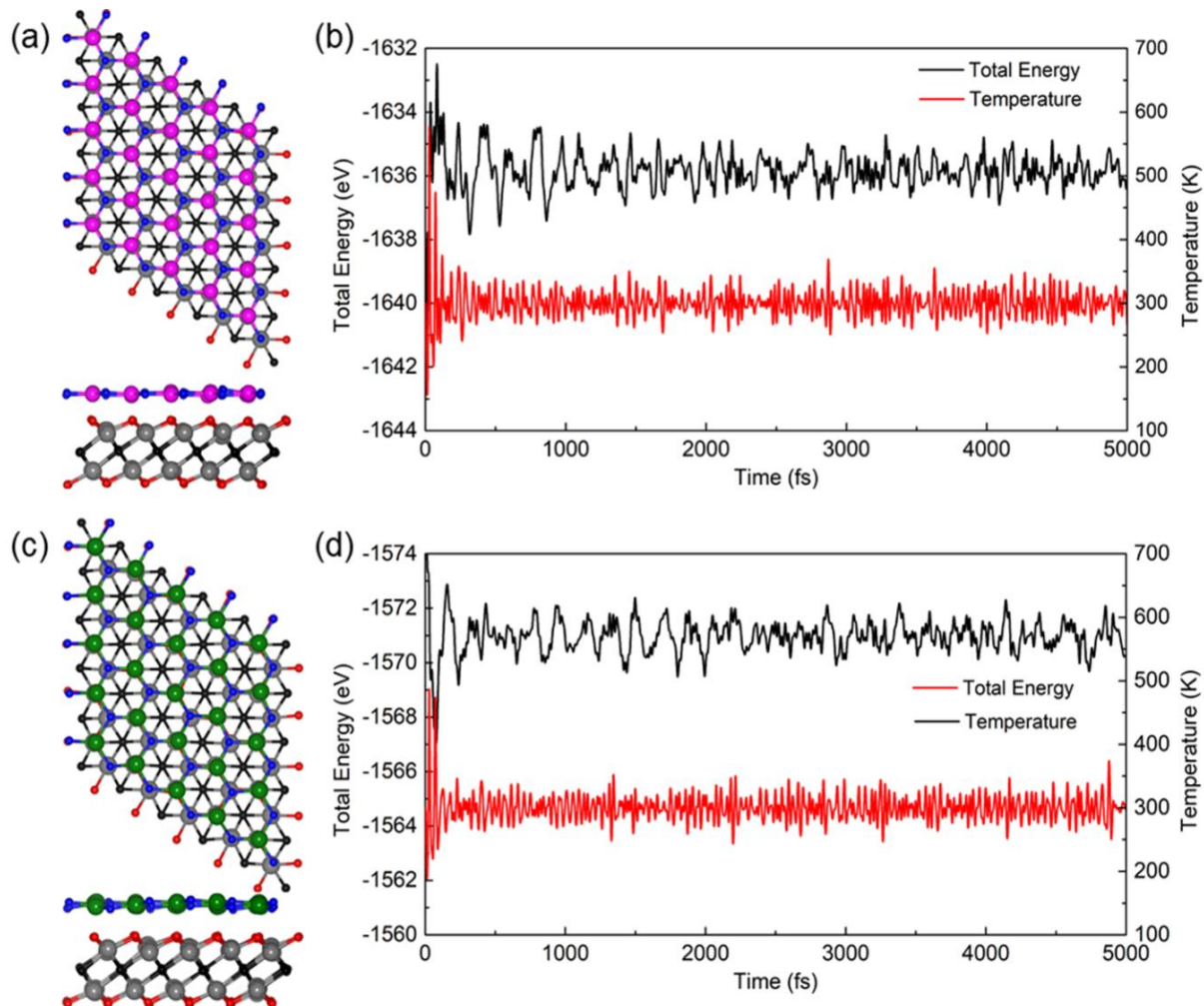

Figure 3. The calculated AIMD snapshots of the (**a**) Hf_2CO_2/AlN and (**c**) Hf_2CO_2/GaN vdW heterostructures at 300 K by 5 ps, and the monitoring of the energy and the temperature during the AIMD simulation for the (**b**) Hf_2CO_2/AlN and (**d**) Hf_2CO_2/GaN vdW heterostructures, respectively.

Figure 4a,c show the projected band structure of the MXene/MN vdW heterostructure. It is obvious that Hf_2CO_2/AlN and Hf_2CO_2/GaN heterostructures have an indirect bandgap of 2.006 eV and 1.899 eV, respectively. The gray and red marks represent the band contribution of AlN (or GaN) and Hf_2CO_2 layers, respectively. Therefore, we can see that the CBM and VBM of both MXene/MN vdW heterostructures are donated from the Hf_2CO_2 layer, and the MXene/MN vdW heterostructure shows I-type band structure. In addition, we also investigated the partial density calculation of MXene/MN vdW heterostructures, as shown in Figure 4b,d, which further proves the intrinsic type-I band structure characteristic. The band structures of the MXene/AlN and MXene/GaN vdW heterostructures by all six

different stacking configurations are calculated in Figures S1 and S2, respectively, in the Supplementary Materials.
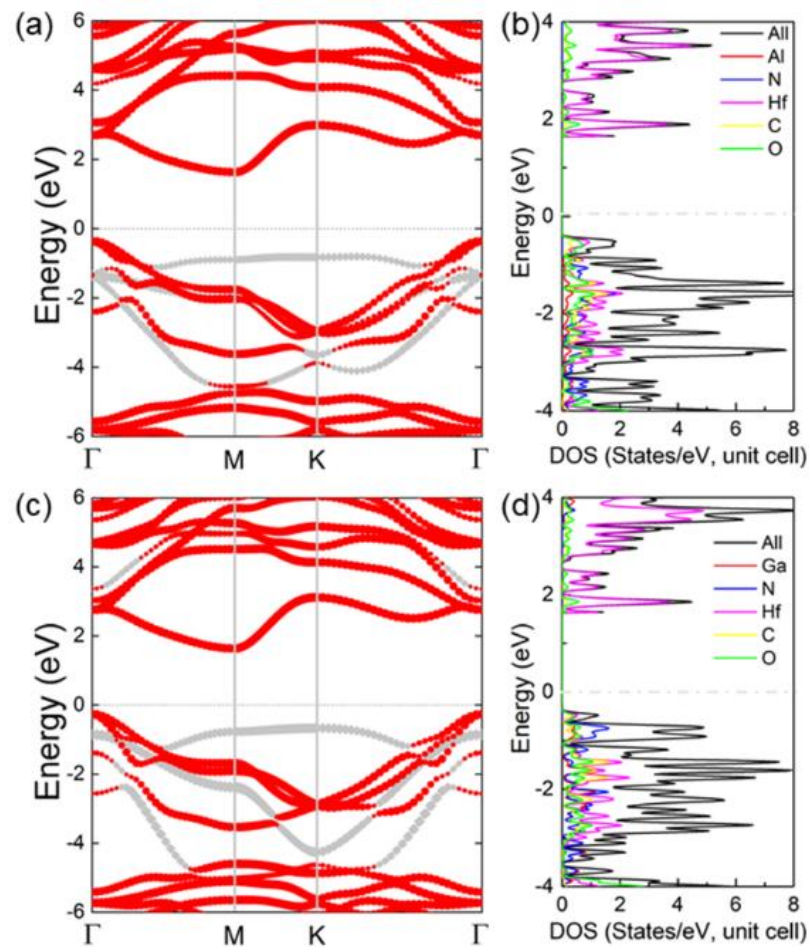

Figure 4. The calculated projected band structure of the (**a**) Hf_2CO_2/AlN and (**c**) Hf_2CO_2/GaN vdW heterostructures; the projected density of states of the (**b**) Hf_2CO_2/AlN and (**d**) Hf_2CO_2/GaN vdW heterostructures. The energy of the Fermi is 0.

In the Hf_2CO_2/MN vdW heterostructure, the bandgap of the Hf_2CO_2 layer is smaller than that of the AlN (or GaN) layer. Additionally, the CBM and VBM of the MXene/MN vdW heterostructure are fixed in the band gap of the Hf_2CO_2 layer, as shown in Figure 5. When some external conditions are applied, the electrons in the wide bandgap of MN will be excited and move to the CBM of MN. At the same time, holes will be induced in the VBM of MN. With the help of conduction band shift (CBO) and valence band shift (VBO), the electrons and holes are excited from the MN layer to the Hf_2CO_2 layer at CBM and VBM, respectively, as shown in Figure 5a. The CBO and VBO of the Hf_2CO_2/AlN (or Hf_2CO_2/GaN) vdW heterostructure are obtained as 2.496 eV (or 0.432eV) and 1.744 eV (or 0.383 eV), respectively. Due to the lower energy, the electrons and holes excited in the Hf_2CO_2 narrow bandgap are prevented from transferring to the MN layer, as shown in Figure 5b [50], suggesting the potential usage of the light-emitting device.
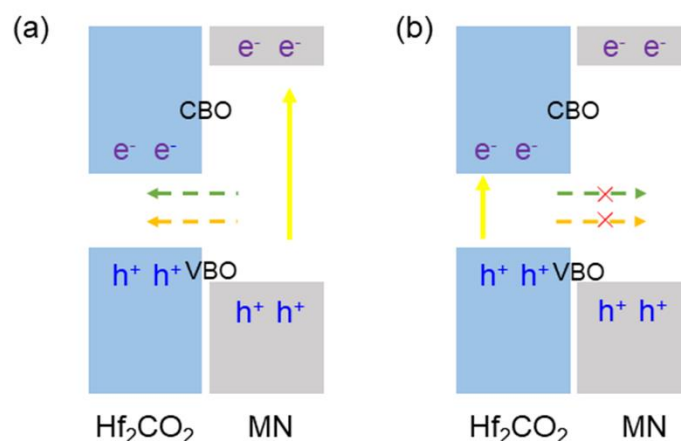
Figure 5. Schematic of the carrier transport in the interface of the type-I band structure for the Hf_2CO_2/MN vdW heterostructure. (**a**) Feasible and (**b**) restricted charge transfer path.

The interesting properties of the interface for the MXene/MN heterostructure were induced by vdW forces, such as the charge difference density ($\Delta\rho$), which is evaluated by:

$$\Delta\rho = \rho_{MXene/MN} - \rho_{MXene} - \rho_{MN} \tag{2}$$

where $\rho_{MXene/MN}$, ρ_{MXene} and ρ_{MN} show the total charge density of the Hf_2CO_2/AlN (or Hf_2CO_2/GaN) vdW heterostructure, monolayered Hf_2CO_2 and AlN (or GaN), respectively. Figure 6a,b show the difference in charge density between the interface in Hf_2CO_2/AlN and Hf_2CO_2/GaN vdW heterostructures. It is obvious that AlN (or GaN) acts as an electron donor in contact with Hf_2CO_2. In addition, the charge density is redistributed in Hf_2CO_2/AlN and Hf_2CO_2/GaN vdW heterostructures, which contributes to the formation of electron-rich and hole-rich regions. It is found that there is charge transfer between the two monolayers. The electron transfer of 0.1513 (or 0.0414) $|e|$ in the Hf_2CO_2/AlN (or Hf_2CO_2/GaN) vdW heterostructure is calculated by the Bader-charge analysis method [103]. In addition, we observed that when Hf_2CO_2 and MN come into contact and reach the equilibrium position, the potential across the interface of the Hf_2CO_2/MN vdW heterostructure decreases to varying degrees due to the charge transfer. The potential of Hf_2CO_2/AlN and Hf_2CO_2/GaN vdW heterostructures decreases by 6.445 eV and 3.752 eV, respectively, which can also be used as an effective driving force to promote carriers in Figure 5. The charge density differences of the MXene/AlN and MXene/GaN vdW heterostructures compared to the other five stacking configurations are obtained by Figures S3 and S4, respectively, in the Supplementary Materials. It is worth noting that the AlN (or GaN) layer still acts as an electron donor for the Hf_2CO_2 layer in the other five stacking configuration heterostructures, and the transferred electrons are calculated in Table S1 in the Supplementary Materials.
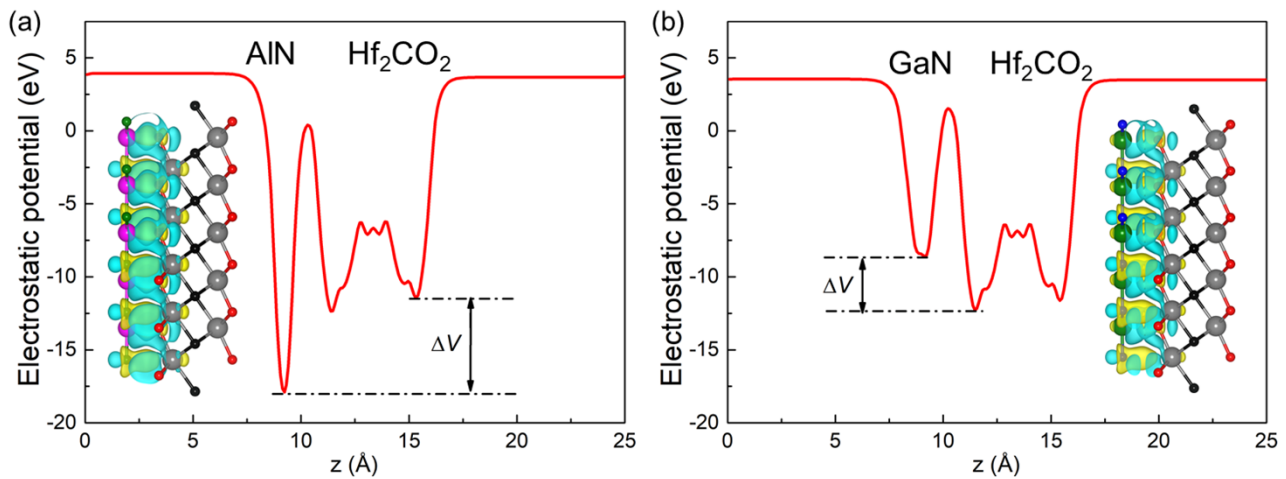
Figure 6. The potential drop for the (**a**) Hf_2CO_2/AlN and (**b**) Hf_2CO_2/GaN vdW heterostructures between the interface. The yellow demonstration shows the gaining of the electrons, while the cyan one means the loss of electrons. $0.0001 \, |e|$ is used for the isosurface level.

The optical absorption capacity of the Hf_2CO_2/MN vdW heterostructure was also investigated. The light absorption capacity of the MXene, MN and the MXene/MN vdW heterostructure is obtained in Figure 7 by the optical absorption spectrum, which is calculated as:

$$\alpha(\omega) = \frac{\sqrt{2}\omega}{c} \left\{ [\varepsilon_1^2(\omega) + \varepsilon_2^2(\omega)]^{\frac{1}{2}} - \varepsilon_1(\omega) \right\}^{\frac{1}{2}} \tag{3}$$

where ω is the angular frequency, α shows the absorption coefficient and c is the speed of light. In addition, $\varepsilon_1(\omega)$ is used to explain the dielectric constant for real parts, and the imaginary one is demonstrated by $\varepsilon_1(\omega)$. It is obvious that the MXene/MN vdW heterostructure possesses the ability to absorb sunlight over a wide range in the visible and NIR regions, which considerably overlaps with the wavelength range of the solar spectrum. Importantly, one can see that the optical performance of the heterostructures is much better than that of AlN and GaN monolayers. Near the wavelength range of visible light, the calculated optical absorption peaks of the Hf_2CO_2/AlN and Hf_2CO_2/GaN vdW heterostructures are 3.627×10^5 cm^{-1} and 3.778×10^5 cm^{-1}, respectively. Furthermore, the Hf_2CO_2/AlN and Hf_2CO_2/GaN vdW heterostructures also possess another peak value obtained by 1.113×10^5 cm^{-1} and 0.962×10^5 cm^{-1}, located at 405 nm and 410 nm, which is higher than that of 0.853×10^5 cm^{-1} for the Hf_2CO_2 monolayer. All these results reveal that both Hf_2CO_2/AlN and Hf_2CO_2/GaN vdW heterostructures have novel optical characteristics. It is worth noting that the calculated optical spectra of these 2D materials in this work do not consider the electron–hole interaction. At present, the *GW*+BSE method has been regarded to be a very crediable method for including the electron–hole interaction, which has been applied in other low-dimensional materials [104,105].
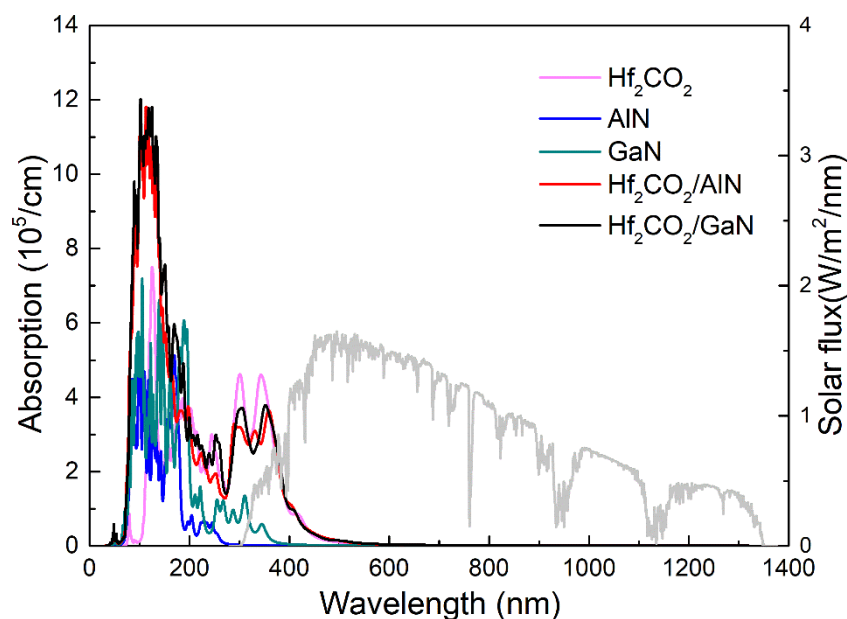
Figure 7. The HSE06 functional obtained optical absorption spectrum for the Hf_2CO_2, AlN, GaN monolayers and Hf_2CO_2/AlN, Hf_2CO_2/GaN vdW heterostructures.

4. Conclusions

The structural and electronic properties of Hf_2CO_2, AlN and GaN monolayers and their heterostructures are investigated by the DFT method. Both Hf_2CO_2/AlN and Hf_2CO_2/GaN vdW heterostructures have strong thermal stability and maintain the original structure at 300 K. Importantly, it is found that both Hf_2CO_2/AlN and Hf_2CO_2/GaN heterostructures are formed by vdW interactions, showing a type-I band structure with a bandgap of 2.006 eV and 1.899 eV, respectively, and they are ideal candidates for light-emitting devices. In addition, the potential of Hf_2CO_2/AlN and Hf_2CO_2/GaN vdW heterostructures is reduced by 6.445 eV and 3.752 eV, respectively. Furthermore, Hf_2CO_2/AlN and Hf_2CO_2/GaN vdW heterostructures have excellent light absorption ability, which can provide theoretical support and technical guidance for future light-emitting device materials. For the efficiency of the light-emitting device, some properties play an important role, such as carrier mobility, lifetime, diffusion and light emission capability, which can be studied further.

References

1. Geim, A.K.; Novoselov, K. The rise of graphene. *Nat. Mater.* **2007**, *6*, 183–191. [CrossRef]
2. Jariwala, D.; Sangwan, V.K.; Lauhon, L.; Marks, T.J.; Hersam, M.C. Carbon nanomaterials for electronics, optoelectronics, photovoltaics, and sensing. *Chem. Soc. Rev.* **2013**, *42*, 2824–2860. [CrossRef]
3. Stoller, M.D.; Park, S.; Zhu, Y.; An, J.; Ruoff, R.S. Graphene-Based Ultracapacitors. *Nano Lett.* **2008**, *8*, 3498–3502. [CrossRef] [PubMed]
4. Wang, J.; Deng, S.; Liu, Z.; Liu, Z. The rare two-dimensional materials with Dirac cones. *Natl. Sci. Rev.* **2015**, *2*, 22–39. [CrossRef]
5. Sun, M.; Tang, W.; Li, S.; Chou, J.-P.; Hu, A.; Schwingenschlögl, U. Molecular doping of blue phosphorene: A first-principles investigation. *J. Phys. Condens. Matter* **2019**, *32*, 055501. [CrossRef]
6. Sun, M.; Schwingenschlögl, U. Unique Omnidirectional Negative Poisson's Ratio in δ-Phase Carbon Monochalcogenides. *J. Phys. Chem. C* **2021**, *125*, 4133–4138. [CrossRef]
7. Sun, M.; Schwingenschlögl, U. δ-CS: A Direct-Band-Gap Semiconductor Combining Auxeticity, Ferroelasticity, and Potential for High-Efficiency Solar Cells. *Phys. Rev. Appl.* **2020**, *14*, 044015. [CrossRef]
8. Palummo, M.; Bernardi, M.; Grossman, J.C. Exciton Radiative Lifetimes in Two-Dimensional Transition Metal Dichalcogenides. *Nano Lett.* **2015**, *15*, 2794–2800. [CrossRef]
9. Bernardi, M.; Palummo, M.; Grossman, J.C. Semiconducting Monolayer Materials as a Tunable Platform for Excitonic Solar Cells. *ACS Nano* **2012**, *6*, 10082–10089. [CrossRef]
10. Chen, H.-Y.; Palummo, M.; Sangalli, D.; Bernardi, M. Theory and Ab Initio Computation of the Anisotropic Light Emission in Monolayer Transition Metal Dichalcogenides. *Nano Lett.* **2018**, *18*, 3839–3843. [CrossRef]
11. Sun, M.; Luo, Y.; Yan, Y.; Schwingenschlögl, U. Ultrahigh Carrier Mobility in the Two-Dimensional Semiconductors B_8Si_4, B_8Ge_4, and B_8Sn_4. *Chem. Mater.* **2021**, *33*, 6475–6483. [CrossRef]
12. Novoselov, K.S.; Geim, A.K.; Morozov, S.V.; Jiang, D.; Zhang, Y.; Dubonos, S.V.; Grigorieva, I.V.; Firsov, A.A. Electric Field Effect in Atomically Thin Carbon Films. *Science* **2004**, *306*, 666–669. [CrossRef]
13. Butler, S.Z.; Hollen, S.; Cao, L.; Cui, Y.; Gupta, J.A.; Gutiérrez, H.R.; Heinz, T.F.; Hong, S.S.; Huang, J.; Ismach, A.F.; et al. Progress, Challenges, and Opportunities in Two-Dimensional Materials Beyond Graphene. *ACS Nano* **2013**, *7*, 2898–2926. [CrossRef]
14. Zheng, Z.; Ren, K.; Huang, Z.; Zhu, Z.; Wang, K.; Shen, Z.; Yu, J. Remarkably improved Curie temperature for two-dimensional CrI_3 by gas molecular adsorption: A DFT study. *Semicond. Sci. Technol.* **2021**, *36*, 075015. [CrossRef]
15. Sun, M.; Yan, Y.; Schwingenschlögl, U. Beryllene: A Promising Anode Material for Na- and K-Ion Batteries with Ultrafast Charge/Discharge and High Specific Capacity. *J. Phys. Chem. Lett.* **2020**, *11*, 9051–9056. [CrossRef]
16. Sun, M.; Chou, J.-P.; Hu, A.; Schwingenschlögl, U. Point Defects in Blue Phosphorene. *Chem. Mater.* **2019**, *31*, 8129–8135. [CrossRef]
17. Sun, M.; Schwingenschlögl, U. Structure Prototype Outperforming MXenes in Stability and Performance in Metal-Ion Batteries: A High Throughput Study. *Adv. Energy Mater.* **2021**, *11*, 2003633. [CrossRef]
18. Li, L.; Yu, Y.; Ye, G.J.; Ge, Q.; Ou, X.; Wu, H.; Feng, D.; Chen, X.H.; Zhang, Y. Black phosphorus field-effect transistors. *Nat. Nanotechnol.* **2014**, *9*, 372–377. [CrossRef] [PubMed]
19. Wu, J.; Mao, N.; Xie, L.; Xu, H.; Zhang, J. Identifying the Crystalline Orientation of Black Phosphorus Using Angle-Resolved Polarized Raman Spectroscopy. *Angew. Chem. Int. Ed.* **2015**, *54*, 2366–2369. [CrossRef] [PubMed]
20. Li, Y.; Yang, S.; Li, J. Modulation of the Electronic Properties of Ultrathin Black Phosphorus by Strain and Electrical Field. *J. Phys. Chem. C* **2014**, *118*, 23970–23976. [CrossRef]
21. Hong, T.; Chamlagain, B.; Lin, W.; Chuang, H.-J.; Pan, M.; Zhou, Z.; Xu, Y.-Q. Polarized photocurrent response in black phosphorus field-effect transistors. *Nanoscale* **2014**, *6*, 8978–8983. [CrossRef] [PubMed]
22. Zhang, S.; Yan, Z.; Shengli, Z.; Chen, Z.; Zeng, H. Atomically Thin Arsenene and Antimonene: Semimetal-Semiconductor and Indirect-Direct Band-Gap Transitions. *Angew. Chem. Int. Ed.* **2015**, *54*, 3112–3115. [CrossRef] [PubMed]
23. Shu, H.; Li, Y.; Niu, X.; Guo, J. Electronic structures and optical properties of arsenene and antimonene under strain and an electric field. *J. Mater. Chem. C* **2017**, *6*, 83–90. [CrossRef]
24. Xu, Y.; Peng, B.; Zhang, H.; Shao, H.; Zhang, R.; Zhu, H. First-principle calculations of optical properties of monolayer arsenene and antimonene allotropes. *Ann. Phys.* **2017**, *529*. [CrossRef]
25. Ersan, F.; Akturk, E.; Ciraci, S. Interaction of Adatoms and Molecules with Single-Layer Arsenene Phases. *J. Phys. Chem. C* **2016**, *120*, 14345–14355. [CrossRef]
26. Dong, M.M.; He, C.; Zhang, W.X. Tunable Electronic Properties of Arsenene and Transition-Metal Dichalcogenide Heterostructures: A First-Principles Calculation. *J. Phys. Chem. C* **2017**, *121*, 22040–22048. [CrossRef]
27. Kamal, C.; Ezawa, M. Arsenene: Two-dimensional buckled and puckered honeycomb arsenic systems. *Phys. Rev. B* **2015**, *91*. [CrossRef]
28. Mogulkoc, Y.; Modarresi, M.; Mogulkoc, A.; Ciftci, Y. Electronic and optical properties of bilayer blue phosphorus. *Comput. Mater. Sci.* **2016**, *124*, 23–29. [CrossRef]
29. Sun, H.; Liu, G.; Li, Q.; Wan, X. First-principles study of thermal expansion and thermomechanics of single-layer black and blue phosphorus. *Phys. Lett. A* **2016**, *380*, 2098–2104. [CrossRef]
30. Mogulkoc, Y.; Modarresi, M.; Mogulkoc, A.; Alkan, B. Electronic and optical properties of boron phosphide/blue phosphorus heterostructures. *Phys. Chem. Chem. Phys.* **2018**, *20*, 12053–12060. [CrossRef]

31. Sun, M.; Hao, Y.; Ren, Q.; Zhao, Y.; Du, Y.; Tang, W. Tuning electronic and magnetic properties of blue phosphorene by doping Al, Si, As and Sb atom: A DFT calculation. *Solid State Commun.* **2016**, *242*, 36–40. [CrossRef]

32. Tsai, D.-S.; Liu, K.-K.; Lien, D.-H.; Tsai, M.-L.; Kang, C.-F.; Lin, C.-A.; Li, L.-J.; He, J.-H. Few-Layer MoS_2 with High Broadband Photogain and Fast Optical Switching for Use in Harsh Environments. *ACS Nano* **2013**, *7*, 3905–3911. [CrossRef] [PubMed]

33. Wang, J.; Shu, H.; Zhao, T.; Liang, P.; Wang, N.; Cao, D.; Chen, X. Intriguing electronic and optical properties of two-dimensional Janus transition metal dichalcogenides. *Phys. Chem. Chem. Phys.* **2018**, *20*, 18571–18578. [CrossRef]

34. Ma, X.; Wu, X.; Wang, H.; Wang, Y. A Janus MoSSe monolayer: A potential wide solar-spectrum water-splitting photocatalyst with a low carrier recombination rate. *J. Mater. Chem. A* **2018**, *6*, 2295–2301. [CrossRef]

35. Liao, C.; Tang, L.; Wang, L.; Li, Y.; Xu, J.; Jia, Y. Low-threshold near-infrared lasing at room temperature using low-toxicity Ag_2Se quantum dots. *Nanoscale* **2020**, *12*, 21879–21884. [CrossRef] [PubMed]

36. Jiang, D.; Ni, C.; Tang, W.; Xiang, N. Numerical simulation of elasto-inertial focusing of particles in straight microchannels. *J. Phys. D Appl. Phys.* **2021**, *54*, 065401. [CrossRef]

37. Sun, M.; Schwingenschlögl, U. B_2P_6: A Two-Dimensional Anisotropic Janus Material with Potential in Photocatalytic Water Splitting and Metal-Ion Batteries. *Chem. Mater.* **2020**, *32*, 4795–4800. [CrossRef]

38. Wang, S.; Ren, C.; Tian, H.; Yu, J.; Sun, M. MoS_2/ZnO van der Waals heterostructure as a high-efficiency water splitting photocatalyst: A first-principles study. *Phys. Chem. Chem. Phys.* **2018**, *20*, 13394–13399. [CrossRef]

39. Kumar, R.; Das, D.; Singh, A.K. C_2N/WS_2 van der Waals type-II heterostructure as a promising water splitting photocatalyst. *J. Catal.* **2018**, *359*, 143–150. [CrossRef]

40. Gong, Y.; Lin, J.; Wang, X.; Shi, G.; Lei, S.; Lin, Z.; Zou, X.; Ye, G.; Vajtai, R.; Yakobson, B.I.; et al. Vertical and in-plane heterostructures from WS_2/MoS_2 monolayers. *Nat. Mater.* **2014**, *13*, 1135–1142. [CrossRef]

41. Zhang, Z.; Zhang, Y.; Xie, Z.; Wei, X.; Guo, T.; Fan, J.; Ni, L.; Tian, Y.; Liu, J.; Duan, L. Tunable electronic properties of an Sb/InSe van der Waals heterostructure by electric field effects. *Phys. Chem. Chem. Phys.* **2019**, *21*, 5627–5633. [CrossRef] [PubMed]

42. Ren, K.; Tang, W.; Sun, M.; Cai, Y.; Cheng, Y.; Zhang, G. A direct Z-scheme PtS_2/arsenene van der Waals heterostructure with high photocatalytic water splitting efficiency. *Nanoscale* **2020**, *12*, 17281–17289. [CrossRef]

43. Ren, K.; Sun, M.; Luo, Y.; Wang, S.; Yu, J.; Tang, W. First-principle study of electronic and optical properties of two-dimensional materials-based heterostructures based on transition metal dichalcogenides and boron phosphide. *Appl. Surf. Sci.* **2019**, *476*, 70–75. [CrossRef]

44. Ren, K.; Wang, S.; Luo, Y.; Xu, Y.; Sun, M.; Yu, J.; Tang, W. Strain-enhanced properties of van der Waals heterostructure based on blue phosphorus and g-GaN as a visible-light-driven photocatalyst for water splitting. *RSC Adv.* **2019**, *9*, 4816–4823. [CrossRef]

45. Ren, K.; Wang, K.; Cheng, Y.; Tang, W.; Zhang, G. Two-dimensional heterostructures for photocatalytic water splitting: A review of recent progress. *Nano Futur.* **2020**, *4*, 032006. [CrossRef]

46. Li, J.; Huang, Z.; Ke, W.; Yu, J.; Ren, K.; Dong, Z. High solar-to-hydrogen efficiency in Arsenene/GaX (X = S, Se) van der Waals heterostructure for photocatalytic water splitting. *J. Alloy. Compd.* **2021**, *866*, 158774. [CrossRef]

47. Din, H.U.; Idrees, M.; Rehman, G.; Nguyen, C.V.; Gan, L.-Y.; Ahmad, I.; Maqbool, M.; Amin, B. Electronic structure, optical and photocatalytic performance of $SiC–MX_2$ (M = Mo, W and X = S, Se) van der Waals heterostructures. *Phys. Chem. Chem. Phys.* **2018**, *20*, 24168–24175. [CrossRef]

48. Williams, K.R.; Diroll, B.T.; Watkins, N.E.; Rui, X.; Brumberg, A.; Klie, R.F.; Schaller, R.D. Synthesis of Type I PbSe/CdSe Dot-on-Plate Heterostructures with Near-Infrared Emission. *J. Am. Chem. Soc.* **2019**, *141*, 5092–5096. [CrossRef]

49. Zheng, W.; Zheng, B.; Jiang, Y.; Yan, C.; Chen, S.; Liu, Y.; Sun, X.; Zhu, C.; Qi, Z.; Yang, T.; et al. Probing and Manipulating Carrier Interlayer Diffusion in van der Waals Multilayer by Constructing Type-I Heterostructure. *Nano Lett.* **2019**, *19*, 7217–7225. [CrossRef] [PubMed]

50. Bellus, M.; Li, M.; Lane, S.; Ceballos, F.; Cui, Q.; Zeng, X.C.; Zhao, H. Type-I van der Waals heterostructure formed by MoS_2 and ReS_2 monolayers. *Nanoscale Horiz.* **2016**, *2*, 31–36. [CrossRef] [PubMed]

51. Dorfs, D.; Franzl, T.; Osovsky, R.; Brumer, M.; Lifshitz, E.; Klar, T.; Eychmüller, A. Type-I and Type-II Nanoscale Heterostructures Based on CdTe Nanocrystals: A Comparative Study. *Small* **2008**, *4*, 1148–1152. [CrossRef]

52. Lei, J.-C.; Zhang, X.; Zhou, Z. Recent advances in MXene: Preparation, properties, and applications. *Front. Phys.* **2015**, *10*, 276–286. [CrossRef]

53. Jiang, Q.; Lei, Y.; Liang, H.; Xi, K.; Xia, C.; Alshareef, H.N. Review of MXene electrochemical microsupercapacitors. *Energy Storage Mater.* **2020**, *27*, 78–95. [CrossRef]

54. Ling, Z.; Ren, C.E.; Zhao, M.-Q.; Yang, J.; Giammarco, J.M.; Qiu, J.; Barsoum, M.W.; Gogotsi, Y. Flexible and conductive MXene films and nanocomposites with high capacitance. *Proc. Natl. Acad. Sci. USA* **2014**, *111*, 16676–16681. [CrossRef] [PubMed]

55. Naguib, M.; Come, J.; Dyatkin, B.; Presser, V.; Taberna, P.-L.; Simon, P.; Barsoum, M.W.; Gogotsi, Y. MXene: A promising transition metal carbide anode for lithium-ion batteries. *Electrochem. Commun.* **2012**, *16*, 61–64. [CrossRef]

56. Wang, S.; Li, B.; Li, L.; Tian, Z.; Zhang, Q.; Chen, L.; Zeng, X.C. Highly efficient N_2 fixation catalysts: Transition-metal carbides M2C (MXenes). *Nanoscale* **2019**, *12*, 538–547. [CrossRef] [PubMed]

57. Xiao, R.; Zhao, C.; Zou, Z.; Chen, Z.; Tian, L.; Xu, H.; Tang, H.; Liu, Q.; Lin, Z.; Yang, X. In situ fabrication of 1D CdS nanorod/2D Ti_3C_2 MXene nanosheet Schottky heterojunction toward enhanced photocatalytic hydrogen evolution. *Appl. Catal. B: Environ.* **2019**, *268*, 118382. [CrossRef]

58. Zhang, X.; Zhang, Z.; Zhou, Z. MXene-based materials for electrochemical energy storage. *J. Energy Chem.* **2018**, *27*, 73–85. [CrossRef]

59. Khazaei, M.; Arai, M.; Sasaki, T.; Chung, C.-Y.; Venkataramanan, N.S.; Estili, M.; Sakka, Y.; Kawazoe, Y. Novel Electronic and Magnetic Properties of Two-Dimensional Transition Metal Carbides and Nitrides. *Adv. Funct. Mater.* **2012**, *23*, 2185–2192. [CrossRef]

60. Zhan, X.; Si, C.; Zhou, J.; Sun, Z. MXene and MXene-based composites: Synthesis, properties and environment-related applications. *Nanoscale Horiz.* **2019**, *5*, 235–258. [CrossRef]

61. He, J.; Ding, G.; Zhong, C.; Li, S.; Li, D.; Zhang, G. Cr_2TiC_2-based double MXenes: Novel 2D bipolar antiferromagnetic semiconductor with gate-controllable spin orientation toward antiferromagnetic spintronics. *Nanoscale* **2018**, *11*, 356–364. [CrossRef] [PubMed]

62. Zhu, B.; Zhang, F.; Qiu, J.; Chen, X.; Zheng, K.; Guo, H.; Yu, J.; Bao, J. A novel Hf_2CO_2/WS_2 van der Waals heterostructure as a potential candidate for overall water splitting photocatalyst. *Mater. Sci. Semicond. Process.* **2021**, *133*, 105947. [CrossRef]

63. Gandi, A.N.; Alshareef, H.N.; Schwingenschlögl, U. Thermoelectric Performance of the MXenes M_2CO_2 (M = Ti, Zr, or Hf). *Chem. Mater.* **2016**, *28*, 1647–1652. [CrossRef]

64. Sharma, V.; Kumar, A.; Krishnan, V. Two-dimensional MXene-based heterostructures for photocatalysis. In *Handbook of Smart Photocatalytic Materials*; Elsevier: Amsterdam, The Netherlands, 2020; pp. 247–267. [CrossRef]

65. Guo, Z.; Miao, N.; Zhou, J.; Sa, B.; Sun, Z. Strain-mediated type-I/type-II transition in MXene/Blue phosphorene van der Waals heterostructures for flexible optical/electronic devices. *J. Mater. Chem. C* **2016**, *5*, 978–984. [CrossRef]

66. Fu, C.-F.; Li, X.; Luo, Q.; Yang, J. Two-dimensional multilayer M_2CO_2(M = Sc, Zr, Hf) as photocatalysts for hydrogen production from water splitting: A first principles study. *J. Mater. Chem. A* **2017**, *5*, 24972–24980. [CrossRef]

67. Li, S.; Li, X.; Zhang, R.; Cui, H. Strain-tunable electronic properties and optical properties of Hf_2CO_2 MXene. *Int. J. Quantum Chem.* **2020**, *120*. [CrossRef]

68. Wang, Y.; Ma, S.; Wang, L.; Jiao, Z. A novel highly selective and sensitive NH_3 gas sensor based on monolayer Hf_2CO_2. *Appl. Surf. Sci.* **2019**, *492*, 116–124. [CrossRef]

69. Bacaksiz, C.; Sahin, H.; Ozaydin, H.D.; Horzum, S.; Senger, T.; Peeters, F.M. Hexagonal AlN: Dimensional-crossover-driven band-gap transition. *Phys. Rev. B* **2015**, *91*, 085430. [CrossRef]

70. Bai, Y.; Deng, K.; Kan, E. Electronic and magnetic properties of an AlN monolayer doped with first-row elements: A first-principles study. *RSC Adv.* **2015**, *5*, 18352–18358. [CrossRef]

71. Zhang, C.-W. First-principles study on electronic structures and magnetic properties of AlN nanosheets and nanoribbons. *J. Appl. Phys.* **2012**, *111*, 43702. [CrossRef]

72. Zhang, C.-W.; Zheng, F.-B. First-principles prediction on electronic and magnetic properties of hydrogenated AlN nanosheets. *J. Comput. Chem.* **2011**, *32*, 3122–3128. [CrossRef]

73. Xu, C.; Xue, L.; Yin, C.; Wang, G. Formation and photoluminescence properties of AlN nanowires. *Phys. Status solidi (a)* **2003**, *198*, 329–335. [CrossRef]

74. Xu, D.; He, H.; Pandey, R.; Karna, S.P. Stacking and electric field effects in atomically thin layers of GaN. *J. Phys. Condens. Matter* **2013**, *25*, 345302. [CrossRef] [PubMed]

75. Chen, Q.; Hu, H.; Chen, X.; Wang, J. Tailoring band gap in GaN sheet by chemical modification and electric field: Ab initio calculations. *Appl. Phys. Lett.* **2011**, *98*, 053102. [CrossRef]

76. Wang, W.; Zheng, Y.; Li, X.; Li, Y.; Zhao, H.; Huang, L.; Yang, Z.; Zhang, X.; Li, G. 2D AlN Layers Sandwiched Between Graphene and Si Substrates. *Adv. Mater.* **2018**, *31*, e1803448. [CrossRef]

77. Taniyasu, Y.; Kasu, M.; Makimoto, T. An aluminium nitride light-emitting diode with a wavelength of 210 nanometres. *Nat. Cell Biol.* **2006**, *441*, 325–328. [CrossRef]

78. Lee, S.; Kim, D.Y. Characteristics of ZnO/GaN heterostructure formed on GaN substrate by sputtering deposition of ZnO. *Mater. Sci. Eng. B* **2007**, *137*, 80–84. [CrossRef]

79. McDermott, E.J.; Kurmaev, E.Z.; Boyko, T.D.; Finkelstein, L.D.; Green, R.J.; Maeda, K.; Domen, K.; Moewes, A. Structural and Band Gap Investigation of GaN:ZnO Heterojunction Solid Solution Photocatalyst Probed by Soft X-ray Spectroscopy. *J. Phys. Chem. C* **2012**, *116*, 7694–7700. [CrossRef]

80. Cui, Z.; Li, E.; Ke, X.; Zhao, T.; Yang, Y.; Ding, Y.; Liu, T.; Qu, Y.; Xu, S. Adsorption of alkali-metal atoms on GaN nanowires photocathode. *Appl. Surf. Sci.* **2017**, *423*, 829–835. [CrossRef]

81. Liao, J.; Sa, B.; Zhou, J.; Ahuja, R.; Sun, Z. Design of High-Efficiency Visible-Light Photocatalysts for Water Splitting: MoS_2/AlN(GaN) Heterostructures. *J. Phys. Chem. C* **2014**, *118*, 17594–17599. [CrossRef]

82. Lou, P.; Lee, J.Y. GeC/GaN vdW Heterojunctions: A Promising Photocatalyst for Overall Water Splitting and Solar Energy Conversion. *ACS Appl. Mater. Interfaces* **2020**, *12*, 14289–14297. [CrossRef]

83. Capelle, K. A bird's-eye view of density-functional theory. *Braz. J. Phys.* **2006**, *36*, 1318–1343. [CrossRef]

84. Grimme, S.; Antony, J.; Ehrlich, S.; Krieg, H. A consistent and accurate ab initio parametrization of density functional dispersion correction (DFT-D) for the 94 elements H-Pu. *J. Chem. Phys.* **2010**, *132*, 154104. [CrossRef] [PubMed]

85. Kresse, G.; Furthmüller, J. Efficiency of ab-initio total energy calculations for metals and semiconductors using a plane-wave basis set. *Comput. Mater. Sci.* **1996**, *6*, 15–50. [CrossRef]

86. Kresse, G.; Furthmüller, J. Efficient iterative schemes for ab initio total-energy calculations using a plane-wave basis set. *Phys. Rev. B* **1996**, *54*, 11169–11186. [CrossRef] [PubMed]

87. Heyd, J.; Peralta, J.; Scuseria, G.E.; Martin, R.L. Energy band gaps and lattice parameters evaluated with the Heyd-Scuseria-Ernzerhof screened hybrid functional. *J. Chem. Phys.* **2005**, *123*, 174101. [CrossRef]

88. Ren, K.; Wang, S.; Luo, Y.; Chou, J.-P.; Yu, J.; Tang, W.; Sun, M. High-efficiency photocatalyst for water splitting: A Janus MoSSe/XN (X = Ga, Al) van der Waals heterostructure. *J. Phys. D Appl. Phys.* **2020**, *53*, 185504. [CrossRef]

89. Singh, A.; Mathew, K.; Zhuang, H.L.; Hennig, R.G. Computational Screening of 2D Materials for Photocatalysis. *J. Phys. Chem. Lett.* **2015**, *6*, 1087–1098. [CrossRef]

90. Voinova, V.V.; Selivanov, N.A.; Plyushchenko, I.V.; Vokuev, M.F.; Bykov, A.Y.; Klyukin, I.N.; Novikov, A.S.; Zhdanov, A.P.; Grigoriev, M.S.; Rodin, I.A.; et al. Fused 1,2-Diboraoxazoles Based on *closo*-Decaborate Anion–Novel Members of Diboroheterocycle Class. *Molecules* **2021**, *26*, 248. [CrossRef]

91. Adonin, S.A.; Bondarenko, M.A.; Novikov, A.S.; Sokolov, M.N. Halogen Bonding in Isostructural Co(II) Complexes with 2-Halopyridines. *Crystals* **2020**, *10*, 289. [CrossRef]

92. Soldatova, N.S.; Suslonov, V.V.; Kissler, T.Y.; Ivanov, D.M.; Novikov, A.S.; Yusubov, M.S.; Postnikov, P.S.; Kukushkin, V.Y. Halogen Bonding Provides Heterooctameric Supramolecular Aggregation of Diaryliodonium Thiocyanate. *Crystals* **2020**, *10*, 230. [CrossRef]

93. Nenajdenko, V.; Shikhaliyev, N.; Maharramov, A.; Bagirova, K.; Suleymanova, G.; Novikov, A.; Khrustalev, V.; Tskhovrebov, A. Halogenated Diazabutadiene Dyes: Synthesis, Structures, Supramolecular Features, and Theoretical Studies. *Molecules* **2020**, *25*, 5013. [CrossRef] [PubMed]

94. Mikherdov, A.; Novikov, A.; Kinzhalov, M.; Zolotarev, A.; Boyarskiy, V. Intra-/Intermolecular Bifurcated Chalcogen Bonding in Crystal Structure of Thiazole/Thiadiazole Derived Binuclear (Diaminocarbene)Pd[II] Complexes. *Crystals* **2018**, *8*, 112. [CrossRef]

95. Kryukova, M.A.; Sapegin, A.V.; Novikov, A.S.; Krasavin, M.; Ivanov, D.M. New Crystal Forms for Biologically Active Compounds. Part 1: Noncovalent Interactions in Adducts of Nevirapine with XB Donors. *Crystals* **2019**, *9*, 71. [CrossRef]

96. Kryukova, M.A.; Sapegin, A.V.; Novikov, A.S.; Krasavin, M.; Ivanov, D.M. New Crystal Forms for Biologically Active Compounds. Part 2: Anastrozole as N-Substituted 1,2,4-Triazole in Halogen Bonding and Lp-π Interactions with 1,4-Diiodotetrafluorobenzene. *Crystals* **2020**, *10*, 371. [CrossRef]

97. Ostras', A.S.; Ivanov, D.M.; Novikov, A.S.; Tolstoy, P.M. Phosphine Oxides as Spectroscopic Halogen Bond Descriptors: IR and NMR Correlations with Interatomic Distances and Complexation Energy. *Molecules* **2020**, *25*, 1406. [CrossRef]

98. Bolotin, D.S.; Il'In, M.V.; Suslonov, V.V.; Novikov, A.S. Symmetrical Noncovalent Interactions Br⋯Br Observed in Crystal Structure of Exotic Primary Peroxide. *Symmetry* **2020**, *12*, 637. [CrossRef]

99. Klyukin, I.; Vlasova, Y.; Novikov, A.; Zhdanov, A.; Zhizhin, K.; Kuznetsov, N. Theoretical Study of *closo*-Borate Anions $[B_nH_n]^{2-}$ (*n* = 5–12): Bonding, Atomic Charges, and Reactivity Analysis. *Symmetry* **2021**, *13*, 464. [CrossRef]

100. Chen, X.; Tian, F.; Persson, C.; Duan, W.; Chen, N.-X. Interlayer interactions in graphites. *Sci. Rep.* **2013**, *3*, 3046. [CrossRef]

101. Björkman, T.; Guļāns, A.; Krasheninnikov, A.; Nieminen, R.M. van der Waals Bonding in Layered Compounds from Advanced Density-Functional First-Principles Calculations. *Phys. Rev. Lett.* **2012**, *108*, 235502. [CrossRef]

102. Nosé, S. A unified formulation of the constant temperature molecular dynamics methods. *J. Chem. Phys.* **1984**, *81*, 511–519. [CrossRef]

103. Tang, W.; Sanville, E.; Henkelman, G. A grid-based Bader analysis algorithm without lattice bias. *J. Phys. Condens. Matter* **2009**, *21*, 084204. [CrossRef] [PubMed]

104. Bernardi, M.; Palummo, M.; Grossman, J.C. Extraordinary Sunlight Absorption and One Nanometer Thick Photovoltaics Using Two-Dimensional Monolayer Materials. *Nano Lett.* **2013**, *13*, 3664–3670. [CrossRef] [PubMed]

105. Bruno, M.; Palummo, M.; Marini, A.; Del Sole, R.; Ossicini, S. From Si Nanowires to Porous Silicon: The Role of Excitonic Effects. *Phys. Rev. Lett.* **2007**, *98*, 036807. [CrossRef] [PubMed]